



# The information on halo properties contained in spectroscopic observations of late-type galaxies

Tariq Yasin <sup>1</sup>\*, Harry Desmond <sup>2</sup>, Julien Devriendt<sup>1</sup> and Adrianne Slyz<sup>1</sup>

<sup>1</sup>*Astrophysics, University of Oxford, Denys Wilkinson Building, Keble Road, Oxford OX1 3RH, UK*

<sup>2</sup>*Institute of Cosmology & Gravitation, University of Portsmouth, Dennis Sciama Building, Portsmouth PO1 3FX, UK*

Accepted 2023 July 20. Received 2023 July 16; in original form 2022 November 15

## ABSTRACT

Rotation curves are the key observational manifestation of the dark matter distribution around late-type galaxies. In a halo model context, the precision of constraints on halo parameters is a complex function of properties of the measurements as well as properties of the galaxy itself. Forthcoming surveys will resolve rotation curves to varying degrees of precision, or measure their integrated effect in the H I linewidth. To ascertain the relative significance of the relevant quantities for constraining halo properties, we study the information on halo mass and concentration as quantified by the Kullback–Leibler divergence of the kinematics-informed posterior from the uninformative prior. We calculate this divergence as a function of the different types of spectroscopic observation, properties of the measurement, galaxy properties, and auxiliary observational data on the baryonic components. Using the SPARC (Spitzer Photometry & Accurate Rotation Curves) sample, we find that fits to the full rotation curve exhibit a large variation in information gain between galaxies, ranging from  $\sim 1$  to  $\sim 11$  bits. The variation is predominantly caused by the vast differences in the number of data points and the size of velocity uncertainties between the SPARC galaxies. We also study the relative importance of the minimum H I surface density probed and the size of velocity uncertainties on the constraining power on the inner halo density slope, finding the latter to be significantly more important. We spell out the implications of these results for the optimization of galaxy surveys aiming to constrain galaxies’ dark matter distributions, highlighting the need for precise velocity measurements.

**Key words:** galaxies: kinematics and dynamics – galaxies: statistics – dark matter.

## 1 INTRODUCTION

In the standard model of cosmology, dark matter clusters under the action of gravity to form virialized, approximately spherical structures known as haloes. Galaxy formation occurs when baryons fall into their deep potential wells, cooling and condensing to form stars. Constraining the relationship between galaxies and their dark matter haloes, the ‘galaxy–halo connection’, is an important step to construct a complete theory of galaxy formation (see Wechsler & Tinker 2018, and references therein).

Perhaps the most direct method to measure dark matter halo density profiles is through spectroscopic observations of galaxies’ kinematics. The mass distribution is then inferred by comparing the observed motions of the gas and stars to the motions expected from the observed luminous matter through Newtonian gravity. Late-type galaxies are ideal systems to study, as their stars and gas follow approximately circular orbits that directly trace the underlying potential. Spatially resolved observations are able to measure rotation curves (RCs), the rotational velocity of the stars and gas as a function of radius (e.g. Walter et al. 2008; Ponomareva, Verheijen & Bosma 2016; Lelli, McGaugh & Schombert 2016a). It has been argued that observed correlations between the dark matter and baryons implied by the RCs (e.g. McGaugh, Lelli &

Schombert 2016; McGaugh et al. 2019) cannot be explained in the cold dark matter paradigm. This has led to an abundance of proposed extensions to the standard model, either in the form of new dark matter physics (e.g. Adhikari et al. 2022; Khelashvili, Rudakovskiy & Hossenfelder 2022) or modifications to the theory of gravity (e.g. Milgrom 1983; Burrage, Copeland & Millington 2017; Naik et al. 2019). Improving the precision of constraints on halo properties is therefore also vital to assess the viability of dark matter models. One approach is to compare the halo properties inferred from kinematics to cosmological expectations (e.g. Katz et al. 2017; Li et al. 2020; Posti & Fall 2021; Mancera Piña et al. 2022; Yasin et al. 2022).

The density profile of dark matter is usually constrained by fitting parametrized functions (e.g. Burkert 1995; Navarro, Frenk & White 1997; Di Cintio et al. 2014; Read, Agertz & Collins 2016) to the measured RC. The parameters, which we refer to as the *properties* of the halo, are typically the virial mass, the concentration (a measure of the autocorrelation of dark matter within the halo) and sometimes additional parameters describing the shape of the profile, such as the steepness of the inner slope. The tightness of the constraints on the free parameters is a complex function of the properties of the measurements (e.g. the number of measured RC data points, the uncertainties on the measured velocities, the maximum radius probed), properties of the galaxy (e.g. stellar surface

\* E-mail: [tariq.yasin@physics.ox.ac.uk](mailto:tariq.yasin@physics.ox.ac.uk)

density, gas fraction), and the precision of auxiliary data on the galaxy (inclination, distance, baryon content).

Rotation curves can be measured using a variety of kinematic tracers. Radio telescopes, in either single dish or interferometer configurations, probe atomic hydrogen (H I), which has the advantage of extending far beyond the optical disc for late-type galaxies, into the region where dark matter dominates. The SPARC (Lelli et al. 2016a) data base, the largest of its type, contains H I rotation curves for 175 late-type galaxies. Collated from archival observations, the measurement properties vary greatly between different RCs. For example, the best sampled RC has 120 data points, and the worst sampled has five. In this paper, we use SPARC to study the precision of constraints on halo parameters as a function of measurement and galaxy properties. This will reveal the ways in which future surveys ought to be designed to maximize their constraining power on the dark matter distributions around galaxies.

Other tracers do not probe as far as H I, but have their own advantages. Optical integral field unit (IFU) surveys such as DiscMass (Martinsson et al. 2013), Mapping Nearby Galaxies at APO (MaNGA, Bundy et al. 2014), and SAMI (Croom et al. 2021) use optical emission from ionized gas or stars, which extends only as far as the galaxy’s stellar component, although the resolution is higher than H I surveys. Sub-mm telescopes (again either in single dish or interferometric configurations) can be used to probe the molecular CO gas disc, which usually extends to 50–70 per cent of the radius of the stellar disc (e.g. Lang et al. 2020).

Future and current surveys H I are seeking to study larger, statistically representative samples of galaxies (e.g. Oosterloo, Verheijen & van Cappellen 2010; Maddox et al. 2021) and galaxies at larger distances. For example, MIGHTEE-HI is an ongoing blind survey that will measure RCs out to  $z = 0.5$ . Due to the further distances, the RCs are sampled more coarsely than in nearby catalogues such as SPARC (Ponomareva et al. 2021). RCs can be measured to lower radius but higher redshift using optical (Di Teodoro, Fraternali & Miller 2016; Stott et al. 2016) and sub-mm (Jones et al. 2021; Lelli et al. 2021, 2023) instruments. Strongly lensed galaxies can also be used to increase the distance probed (e.g. Rizzo et al. 2021).

Finally all of the methods described above can be used to obtain spatially integrated spectra, which requires significantly less integration time and so can be obtained for orders of magnitude more galaxies. Current surveys such as Arecibo Legacy Fast ALFA (ALFALFA, Haynes et al. 2018), and future surveys such as the Widefield ASKAP L-band Legacy All-sky Blind survey (WAL-LABY, Koribalski et al. 2020; Deg et al. 2022), Commensal Radio Astronomy FasT Survey (CRAFTS, Zhang et al. 2020), and the Square Kilometre Array (SKA, Yahya et al. 2015) will measure the spatially integrated H I emission for cosmological volumes of galaxies.

These different observational techniques and tracers will measure rotation velocities with varying precision and will probe different parts of the RC. The constraining power of these different types of kinematic measurement on halo properties has never been studied in detail. To begin investigation of this question, we study here the information content contained in different parts of the RCs of the SPARC galaxies. This is achieved by constraining halo properties using the RC summary statistics recorded in SPARC, each of which characterize a particular part of the RC. These statistics are  $V_{\text{flat}}$ , the speed of the flat part of the rotation curve,  $V_{\text{max}}$ , the peak rotational speed and  $V_{2.2}$ , the circular velocity at 2.2 times the disc exponential scale length, and  $W_{p20}$  the width of the spatially integrated H I line profile at 20 per cent of the peak flux.

RC summary statistics have previously been utilized extensively in the study of the Tully–Fisher relation (TFR), the tight empirical relationship between the mass or luminosity of a galaxy and some measure of its rotational velocity. The TFR was first defined using H I linewidth (Tully & Fisher 1977), and later studies have used  $V_{\text{max}}$  (Conselice et al. 2004),  $V_{2.2}$  (Courteau 1997) or  $V_{\text{flat}}$  (McGaugh 2005; Ponomareva et al. 2018). Recently Lelli et al. (2019, henceforth L19) compared the baryonic TFR (McGaugh et al. 2000; McGaugh 2005; Iorio et al. 2016; Lelli, McGaugh & Schombert 2016b) produced by different summary statistics of the RC, as well as the H I line width, for the SPARC galaxies. The study of the dark matter halo constraints offered by these summary statistics is also interesting in this context.

A velocity summary statistic is sensitive only to the enclosed dynamical mass within the radius it probes (which can be estimated as  $M \sim V^2 R/G$ , Caserano & Shostak 1980). Hence, although summary statistics do provide information on halo mass and concentration (once a profile is assumed), the constraints are relatively weak due to the degeneracy between the two parameters: the same enclosed mass can be generated by either a high mass, low concentration or a low mass, high concentration halo. The degeneracy can be broken to some extent by assuming a halo mass–concentration relation from simulations (e.g. Posti, Fraternali & Marasco 2019), but the extent to which these relationships are obeyed by real haloes is uncertain (Dutton & Macciò 2014; Katz et al. 2017; Li et al. 2020; Mancera Piña et al. 2022). For example, due to assembly bias (Dalal et al. 2008), we do not expect a population of relatively isolated, late-type galaxies such as those found in SPARC to follow an identical mass–concentration relationship to that of all the haloes in a simulation.

Without an informative prior linking mass and concentration, the kinematic data alone can sometimes not exclude unphysical scenarios such as low-mass galaxies having cluster mass haloes. Studying the degenerate posterior in mass–concentration can still yield insight however. The constraints from summary statistics can be compared and/or combined with other pieces of information, such as abundance matching (Yasin et al. 2022), optical kinematics (proposed by Taranu et al. 2017) or weak lensing data (Shajib et al. 2021, for Sloan Digital Sky Survey velocity dispersions). Therefore in this study we choose to analyse the constraining power in the mass–concentration plane offered by the different types of measurements without applying a mass–concentration prior, although we discuss the effects this would have in Section 4.1. We quantify the precision of constraints on halo properties using the Kullback–Leibler divergence ( $D_{\text{KL}}$ , Kullback & Leibler 1951) of the posterior from the prior, a measure of information gain based on information theory. We study the information gain of the 2D total mass–concentration posterior (where total mass is equal to the halo mass plus the galaxy mass). We use total mass rather than halo mass, because the lower bound of the prior on total mass can be naturally set to the galaxy mass, whereas the halo mass, when sampled logarithmically (as is computationally necessary), has no natural lower bound. Our method could equally be applied to additional parameters describing shape. By quantifying the information gain on these halo properties when using either the full RCs, H I line widths or summary statistics to constrain the kinematic model, we aim to answer the following questions:

- (i) How does the information content depend on properties of the measurement such as velocity uncertainties, the minimum H I surface density probed and auxiliary data on galaxy parameters.
- (ii) How does the information content depend on galaxy properties?
- (iii) How much information is contained in different summary statistics compared to the full RC?

(iv) How much information is there in integrated HI measurements relative to more expensive, spatially resolved measurements?

To answer the first two questions we will construct a predictive model for  $D_{\text{KL}}$  given the galaxy and measurement properties as input. The paper is structured as follows: Section 2 describes the SPARC data. Section 3 describes the Bayesian models for inferring halo properties from the observations. In Section 4, we present the information content as a function of different types of observations, measurement properties, and galaxy properties. We discuss the implications of our results in Section 5, and conclude in Section 6. We define the halo mass  $M_{\text{halo}}$  using the overdensity condition  $\Delta_{\text{vir}} = 178$  of Bryan & Norman (1998). All logarithms are base-10 unless stated otherwise.

## 2 OBSERVATIONAL DATA

SPARC<sup>1</sup> (Lelli et al. 2016a) is a data base of rotation curves for 175 late-type galaxies, collated from archival resolved HI observations. In addition, 56 galaxies have hybrid rotation curves with high-resolution H $\alpha$  data in the inner parts. Each galaxy has Spitzer photometry (Schombert & McGaugh 2014) at 3.6  $\mu\text{m}$ , a band in which the mass-to-light ratio is relatively constant (Schombert, McGaugh & Lelli 2018), which reduces the disc-halo degeneracy in kinematic analyses. The distributions of the stars and gas (*mass models*) are provided in the form of the contribution of each component to the circular velocity as a function of radius. We also utilize the HI surface density ( $\Sigma_{\text{HI}}$ ) as a function of radius (F. Lelli, private communication) in our analysis. The SPARC galaxies span a wide range in luminosity ( $10^7$  to  $10^{12} L_{\odot}$ ), surface brightness ( $\sim 5$  to  $\sim 5000 L_{\odot} \text{pc}^{-2}$ ), HI mass ( $\sim 10^7$  to  $10^{10.6} M_{\odot}$ ), and morphological type (S0 to Im/BCD).

L19 calculate the RC summary statistics  $V_{\text{flat}}$ ,  $V_{\text{max}}$ ,  $V_{2.2}$ , and their associated errors for a subset of SPARC sample with cuts on properties such as  $i$  and number of data points. We use their definitions to calculate  $V_{\text{max}}$  and  $V_{2.2}$  for the whole sample, but we calculate  $V_{\text{flat}}$  using our own definition, which we describe in Section 3.2. The definitions of the velocity measurements are summarized in Table 1. L19 also compile HI linewidths from archival data for various different definitions. We choose to use  $W_{p20}$ , the width at 20 percent of the peak flux, as it is available for the most galaxies. Unlike L19, we do not include the contribution from inclination to the observational uncertainties on the summary statistics and  $W_{p20}$ , as inclination is a free parameter in our inference.

## 3 METHODS

### 3.1 Rotation curve model

Dark matter halo properties are inferred by fitting a parametrized halo profile to the observational data. Different halo profiles have been studied extensively in literature but a clear picture has yet to emerge of the relationship between the properties of a galaxy and the shape of its halo (Katz et al. 2017; Li et al. 2020). The haloes in dark matter-only simulations were found to have a universal profile dubbed Navarro–Frenk–White (NFW) (Navarro et al. 1997), but profiles motivated by hydrodynamical simulations, that interpolate between a cusp and a core based on galaxy/halo properties (Di Cintio et al. 2014; Read et al. 2016), have been found to fit the SPARC data better than the NFW profile (Katz et al. 2017; Li et al. 2020). However cores have

been observed in high mass systems (Collett et al. 2017), including for the SPARC galaxies (Li et al. 2019, 2022), which is against the mass-dependent behaviour of the supernova-induced core flattening predicted by the aforementioned hydrodynamical simulations. On the other hand many studies have found NFW haloes to be good fits to clusters and weak lensing data for high-mass galaxies (e.g. Mandelbaum et al. 2016), and some have argued that the inference of cores from 21-cm rotation curve observations may be due to systematics (Roper et al. 2022). In light of this uncertainty we choose to study the NFW and Burkert (Burkert 1995) profiles as representative examples of a cusped and cored profiles respectively. Due to the preference of most SPARC galaxies for cores using our modelling procedure (in agreement with Li et al. 2020, although see Posti et al. 2019 for a different analysis), we present our results primarily for the Burkert profile.

The NFW density profile is

$$\rho_{\text{NFW}}(r) = \frac{\rho_s}{\left(\frac{r}{r_s}\right) \left[1 + \left(\frac{r}{r_s}\right)\right]^2}, \quad (1)$$

where  $r_s$  is a scale radius and  $\rho_s$  a characteristic density. The enclosed mass at radius  $r$  is

$$M_{\text{NFW}}(r) = 4\pi\rho_s r_s^3 \left[ \ln(1+x) - \frac{x}{1+x} \right], \quad (2)$$

where  $x \equiv r/r_s$ . The Burkert density profile is

$$\rho_{\text{Burkert}}(r) = \frac{\rho_s}{\left(1 + \frac{r}{r_s}\right) \left[1 + \left(\frac{r}{r_s}\right)^2\right]}, \quad (3)$$

and the enclosed mass is given by

$$M_{\text{Burkert}}(r) = 2\pi\rho_s r_s^3 \left[ \frac{1}{2} \ln(1+x^2) + \ln(1+x) - \arctan(x) \right]. \quad (4)$$

We also analyse how well observations can constrain a shape parameter for the inner halo by studying the generalized-NFW profile (gNFW, e.g. Umetsu et al. 2011), with density

$$\rho_{\text{gNFW}}(r) = \frac{\rho_s}{\left(\frac{r}{r_s}\right)^{\alpha} \left[1 + \left(\frac{r}{r_s}\right)\right]^{3-\alpha}}. \quad (5)$$

This reduces to NFW for  $\alpha = 1$ . The mass enclosed is given by

$$M_{\text{gNFW}}(r) = 4\pi\rho_s r_s^3 [B(x/(1+x), 3-\alpha, 0)], \quad (6)$$

where  $B(z; a, b) \equiv \int_0^z u^{a-1} (1-u)^{b-1} du$ .

Typically rotation curve measurements extend to only a small fraction of the virial radius (e.g. Katz et al. 2019). Therefore constraining halo mass requires a large extrapolation. Whilst gNFW, NFW, and Burkert differ in shape towards the centre, at large radii they all decline as  $\rho \propto 1/r^3$ , so the comparison between the inferred masses is fair.

The circular speed due to the dark matter at radius  $r$  is  $V_{\text{DM}} = \sqrt{GM_{\text{DM}}(r)/r}$ . It is conveniently expressed in terms of  $M_{\text{halo}}$ , the virial velocity ( $V_{\text{halo}}$ ), and the virial radius ( $R_{\text{halo}}$ ),

$$\frac{V_{\text{DM}}(r)}{V_{\text{halo}}} = \sqrt{\frac{M_{\text{DM}}(r) R_{\text{halo}}}{M_{\text{halo}} r}}, \quad (7)$$

where  $V_{\text{halo}} \equiv \sqrt{GM_{\text{halo}}/R_{\text{halo}}}$ . Concentration is commonly defined based on the radius at which the logarithmic slope of the density profile is  $-2$  ( $r_{-2}$ , which for NFW is equal to  $r_s$ )

$$c = \frac{R_{\text{halo}}}{r_{-2}}. \quad (8)$$

<sup>1</sup><http://astroweb.cwru.edu/SPARC/>

**Table 1.** The summary statistics of the full rotation curve and H I linewidth definition used in this paper.

Measurement	Interpretation	Sample size
Full RC	The full rotation curve.	175
$V_{\text{flat}}$	The velocity of the flat part of the rotation curve. The algorithm to identify the flat part of the rotation curve is listed in Section 3.2 and differs slightly from the definition used in the SPARC data base.	123
$V_{\text{max}}$	The maximum velocity of the rotation curve. If the rotation curve is continuously rising in the observed range then this is the outermost measured point	175
$V_{2.2}$	The velocity at twice the exponential stellar disc scale length. This is found by linearly interpolating between data points on either side of the required radius.	167
$W_{\text{p}20}$	The width of the global H I 21-cm emission line of a galaxy measured at 20 per cent of the peak flux.	148

**Table 2.** The free parameters in our kinematic model, their physical definitions, and their Bayesian priors. We sample all parameters in logarithmic space except inclination and distance.

Parameter	Units	Definition	Prior
$M_{\text{tot}}$	( $M_{\odot}$ )	Total mass $M_{\text{tot}} = M_{\text{halo}} + M_{\text{bar}}$	Flat in range $\log(M_{\text{bar}}/M_{\odot}) < \log(M_{\text{tot}}/M_{\odot}) < 15.5$
$c_{0.1}$	-	Halo concentration, as defined in equation (9)	Flat in range $0.5 < \log c_{0.1} < 2$
$\Upsilon_{\text{disc}}$	( $M_{\odot}/L_{\odot}$ )	Disc mass-to-light ratio	Lognormal ( $\mu = \log(0.5)$ , $\sigma = 0.1$ )
$\Upsilon_{\text{bulge}}$	( $M_{\odot}/L_{\odot}$ )	Bulge mass-to-light ratio	Lognormal ( $\mu = \log(0.7)$ , $\sigma = 0.1$ )
$D$	(Mpc)	Physical distance to galaxy	Gaussian prior from SPARC value and its uncertainty
$i$	(deg)	Inclination ( $0^{\circ}$ face on; $90^{\circ}$ edge on)	Gaussian prior from SPARC value and its uncertainty

Following Yasin et al. (2022) we instead use the definition

$$c_{0.1} = \frac{R_{\text{halo}}}{r_{0.1}}, \quad (9)$$

where  $r_{0.1}$  is the radius enclosing 10 per cent of  $M_{\text{halo}}$ . This definition has three advantages: (1) It can be calculated in simulations by simply counting dark matter particles, rather than fitting a profile; (2)  $r_{0.1}$  is defined for all halo profiles, as it does not require a particular slope; (3) It is not based on the halo's shape, and hence is more intuitive.

Our Bayesian fitting procedure is similar to those of Katz et al. (2017) and Li et al. (2020). As the late-type galaxies studied are rotationally dominated, we assume the rotational speed is equal to the circular speed. We try a non-fiducial model where we add 10  $\text{km s}^{-1}$  in quadrature to all velocities as a crude ‘asymmetric drift’ correction, and find it does not affect our results (see Bureau & Carignan 2002; Oh et al. 2015; Iorio et al. 2016 for a full discussion of asymmetric drift). The total circular speed,  $V_c(r)$  is equal to the sum in quadrature of the circular speed due to the dark matter and each baryonic component (dark matter, gas, stellar disc, stellar bulge)

$$V_c^2(r) = V_{\text{DM}}|V_{\text{DM}}| + \Upsilon_{\text{bulge}}V_{\text{bulge}}|V_{\text{bulge}}| + \Upsilon_{\text{disc}}V_{\text{disc}}|V_{\text{disc}}| + V_{\text{gas}}|V_{\text{gas}}|, \quad (10)$$

where each  $V$  is also a function of  $r$ , and  $\Upsilon_{\text{bulge/disc}}$  is the mass-to-light ratio of the bulge or disc. The latter are tabulated in the SPARC data base for each galaxy. The baryonic mass models depend on the assumed distance as

$$V_{\text{disc,bulge,gas}}(r) \propto \sqrt{D}, \quad (11)$$

and the radius depends on the assumed distance as

$$r \propto D. \quad (12)$$

The model prediction for the line-of-sight rotational speed is found by correcting  $V_c(r)$  for the inclination  $i$  of the galaxy ( $i = 0^{\circ}$  face-on;  $i = 90^{\circ}$  edge-on)

$$V_{\text{pred}}(r) = V_c(r) \sin i. \quad (13)$$

$D$ ,  $i$ ,  $\Upsilon_{\text{disc}}$ , and  $\Upsilon_{\text{bulge}}$  are free parameters in the inference. When fitting to the full RC,  $V_{\text{pred}}(r)$  can be compared directly to the observed RC. For the summary statistics,  $V_{\text{pred}}(r)$  is evaluated at the same radii as the observed data points, and then the same algorithm that was

used to calculate each summary statistic from the observed RC is applied.

### 3.2 Definition of $V_{\text{flat}}$

The algorithm to calculate  $V_{\text{flat}}$  in the SPARC data base (see Lelli, McGaugh & Schombert 2015) starts by defining the outermost observed data point as being the flat part of the RC, and then adds additional points to it iteratively. At each step the next innermost data point at radius  $r_{i-1}$  is added if its speed is within 5 per cent of the mean of the data points already included:

$$\Delta \equiv \frac{|\bar{V} - V_{i-1}|}{\bar{V}} < 0.05. \quad (14)$$

If the difference is greater than 5 per cent the process terminates, and  $V_{\text{flat}}$  is the mean of the points already included. A galaxy is only considered to have a defined  $V_{\text{flat}}$  if the flat part constitutes at least three points when the algorithm terminates. The definition depends on the distance between the points, which means finely sampled RCs can still be considered flat even if they are much steeper than less finely sampled RCs. To lessen this bias we change the condition to a limit on  $\Delta$  per stellar disc scale length ( $R_{\text{disc}}$ ),

$$\frac{\Delta}{(R_i - R_{i-1})/R_{\text{disc}}} < 0.10. \quad (15)$$

The condition is set to 10 per cent per disc scale length so  $V_{\text{flat}}$  is defined for a similar number of galaxies (123) as the original definition (133). Our results are not sensitive to the exact value. For galaxies which meet both the old and new  $V_{\text{flat}}$  definition, the difference between the two values is negligible.

### 3.3 H I linewidth model

The summary statistics  $V_{\text{max}}$ ,  $V_{2.2}$ , and  $V_{\text{flat}}$  can be calculated from the RC alone. To calculate a model  $W_{\text{p}20}$  that can be compared to the observed value, we must calculate a model H I integrated spectrum from the RC and the H I surface density profile. Our method is described and validated in detail in Yasin et al. (2022), but we describe

it here in brief. We use the method of Obreschkow et al. (2009), treating the HI disc as a series of concentric infinitely thin rings each with circular velocity given by  $V_{\text{pred}}(r)$ . We want to calculate the flux observed at the wavelength  $\lambda$  that corresponds to gas with a radial velocity  $V_\lambda$  relative to the kinematic centre of the galaxy. The normalized flux from a single infinitely thin ring of gas is given by

$$\tilde{\psi}(V_\lambda, V_{\text{pred}}) = \begin{cases} \frac{1}{\pi \sqrt{V_{\text{pred}}^2 - V_\lambda^2}} & \text{if } |V_\lambda| < V_{\text{pred}} \\ 0, & \text{otherwise.} \end{cases} \quad (16)$$

We assume the gas has a constant velocity dispersion of  $10 \text{ km s}^{-1}$  (based on observations of local galaxies: Leroy et al. 2008; Mogotsi et al. 2016), which broadens the flux distribution from each ring

$$\psi(V_\lambda, V_{\text{pred}}) = \frac{\sigma_{\text{HI}}^{-1}}{\sqrt{2\pi}} \int_{-\infty}^{+\infty} dV \exp\left[\frac{(V_\lambda - V)^2}{-2\sigma_{\text{HI}}^2}\right] \tilde{\psi}(V, V_{\text{pred}}). \quad (17)$$

The total, integrated flux profile of the galaxy is then obtained by integrating across the whole HI disc:

$$\Psi_{\text{HI}}(V_\lambda) = \frac{2\pi}{M_{\text{HI}}} \int_0^\infty dr r \Sigma_{\text{HI}}(r) \psi(V_\lambda, V_{\text{pred}}(r)). \quad (18)$$

The resulting flux profile is symmetric, so the model  $W_{p20}$  summary statistic can be trivially calculated by finding a peak of the distribution, and moving outwards to larger speed until the flux drops to 20 per cent of the maximum. Although the observed profile may be asymmetric, the important quantity is the width, so this should not bias the results. This is verified for the SPARC sample in Yasin et al. (2022).

### 3.4 Inference

Bayes' theorem is used to calculate the probability of our parameters  $\theta$  condition on our data  $D$  given the model  $\mathcal{M}$ ,

$$\mathcal{P}(\theta|D, \mathcal{M}) = \frac{\mathcal{L}(D|\theta, \mathcal{M})\pi(\theta|\mathcal{M})}{p(D|\mathcal{M})}, \quad (19)$$

where  $\mathcal{L}(D|\theta, \mathcal{M})$  is the likelihood of the data,  $\pi(\theta|\mathcal{M})$  is the prior probability density, and  $p(D|\mathcal{M})$  the marginalized likelihood. For  $V_{\text{flat}}$ ,  $V_{\text{max}}$ ,  $V_{2.2}$ ,  $W_{p20}$ , which consist of a single observation, the likelihood of the data is

$$\mathcal{L}(W_{\text{obs}}|\theta, \mathcal{M}) = \frac{\exp\{-(W_{\text{obs}} - W_{\text{pred}})^2/(2\delta W_{\text{obs}}^2)\}}{\sqrt{2\pi}\delta W_{\text{obs}}}, \quad (20)$$

where  $W_{\text{obs}}$  is the observed velocity summary statistic and  $W_{\text{pred}}$  the model prediction. For the full rotation curve the likelihood is

$$\mathcal{L}(D|\theta, \mathcal{M}) = \prod_i \frac{\exp\{-(V_{i,\text{obs}} - V_{\text{pred}}(r_i))^2/(2\delta V_{i,\text{obs}}^2)\}}{\sqrt{2\pi}\delta V_{i,\text{obs}}}. \quad (21)$$

When fitting with summary statistics we find some galaxies have non-zero posterior probability at  $M_{\text{halo}} = 0$ . Therefore in order to raise the lower limit of the posterior to a finite value we sample  $\log M_{\text{tot}} = \log(M_{\text{halo}} + M_{\text{bar}})$  rather than  $M_{\text{halo}}$  itself, setting the lower bound on its flat prior to be  $\log M_{\text{bar}}$ . A minimum baryonic content for each galaxy regardless of  $\Upsilon$  is ensured by the HI mass, which is relatively well constrained by observations and so is not allowed to vary in our model (apart from through its dependence on distance).

The total free parameters are  $\{M_{\text{tot}}, c_{0.1}, \Upsilon_{\text{disc}}, \Upsilon_{\text{bulge}}, i, D\}$  (summarised in Table 2). The priors on  $\Upsilon_{\text{disc}}$  and  $\Upsilon_{\text{bulge}}$  are lognormal with means of  $\log(0.5)$  and  $\log(0.7)$  respectively, and 0.1 dex scatter (following Li et al. 2020). The priors on  $i$  and  $D$  are normal with mean given by the observed values and scatter by the observational

uncertainties from SPARC. The posterior is sampled using the emcee ensemble sampler (Foreman-Mackey et al. 2013). We set the number of walkers to 200 and the stretch move to  $a = 2$ . To ensure the chain is converged we run the sampler until the chain is at least 50 times the autocorrelation length (Goodman & Weare 2010) in all parameters, or a minimum of 10 000 steps to ensure the posterior is densely sampled to aid in the calculation of  $D_{\text{KL}}$ . The first 25 autocorrelation lengths are discarded as burn-in.

### 3.5 Goodness-of-fit

We wish to examine the dependence of constraining power on the type and precision of the measurements. A nuisance effect is that constraints can be very tight for models that are a poor fit to the data, as a small fraction of parameter space can still have high likelihood relative to the rest of it, even if the absolute value of the likelihood is low for that region (a problem previously identified for rotation curves, e.g. Li et al. 2020).

To exclude galaxies that are poor fits to a particular profile, we examine the distribution of normalized residuals

$$\mathcal{R}_i = \frac{V_{i,\text{obs}} - V_{\text{pred}}(r_i)}{\delta V_{i,\text{obs}}}, \quad (22)$$

evaluated for the  $i$  RC data points of a galaxy. The set of  $\mathcal{R}_i$  should be drawn from a standardized normal distribution if the model is perfect (Andrae, Schulze-Hartung & Melchior 2010; Zentner et al. 2022). We identify galaxies as having poor fits if the probability that the distribution of residuals is drawn from a standardized normal is  $p_{\text{fit}} < 0.05$ , as calculated by the Kolmogorov–Smirnov test (Massey 1951). The probabilistic nature of the test means it is more stringent for better sampled rotation curves, which is desirable as better sampled rotation curves generally give stronger constraints on halo properties. We define a galaxy as overfit if  $p_{\text{fit}} < 0.05$  and the standard deviation of their residuals is less than 1, and underfit if  $p_{\text{fit}} < 0.05$  and the standard deviation of residuals is greater than 1. This procedure finds 23 (14) galaxies to be underfit and 8 (11) overfit for the NFW (Burkert) profile in the fiducial model. These are removed from the sample.

We find that the galaxies for which Burkert is underfit have higher than average mass, but for NFW there is no clear trend with any galaxy property (including inclination). There is no clear trend for overfitting using either halo profile. Finally, removing under/overfit galaxies does not significantly impact the distribution of  $D_{\text{KL}}$  for the sample. This suggests that whether or not the above procedure has identified all poor fits, the issue of poorly fitting galaxies having tight constraints is unlikely to bias our subsequent analysis of  $D_{\text{KL}}$ .

### 3.6 Abundance matching

For reference we also show the information gain on halo properties from abundance matching (AM), an empirical model that matches the haloes in simulations to observed galaxies by positing an approximately monotonic relationship between a halo property (the *proxy*) and a galaxy observable (e.g. Kravtsov et al. 2004; Conroy, Wechsler & Kravtsov 2006). In the simplest model the proxy is halo mass and the galaxy observable is stellar mass or luminosity. We use the proxy of Lehmann et al. (2016) which models assembly bias through the hybrid proxy  $v_\beta := V_{\text{halo}} \left(\frac{v_{\text{max}}}{V_{\text{halo}}}\right)^\beta$ , where  $v_{\text{max}}$  is the maximum circular velocity of the halo and  $V_{\text{halo}}$  is the velocity at the virial radius. The free parameters in the model are the AM scatter  $\sigma_{\text{AM}}$  and  $\beta$ , which they constrain by clustering to  $\beta = 0.57_{-0.27}^{+0.20}$  and

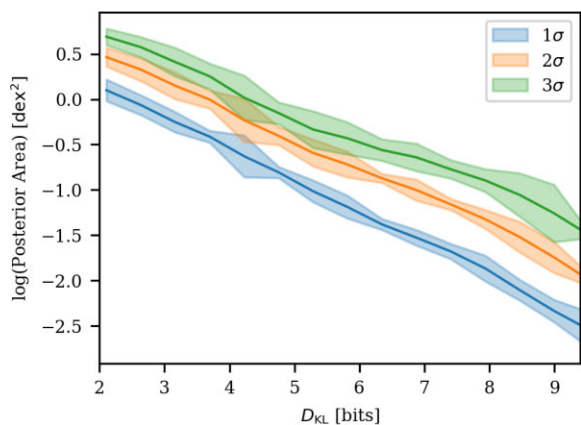


**Figure 1.** The correlation between the KL divergence ( $D_{\text{KL}}$ ) of the posterior from the prior in  $M_{\text{tot}} - c_{0,1}$  space and the area of the 2D posterior (for varying confidence intervals) from fitting Burkert haloes to the full RC for the whole sample of galaxies. The solid lines show the mean posterior area in bin of  $D_{\text{KL}}$  (15 bins total), with the band showing the  $1\sigma$  spread in each bin.  $D_{\text{KL}}$  and posterior size are strongly correlated, with a small scatter due to changing shapes of the posteriors and the prior on  $M_{\text{tot}}$  that is a function of the galaxy's  $M_{\text{bar}}$ .

$\sigma_{\text{AM}} = 0.17_{-0.05}^{+0.03}$ . We calculate the posterior on mass–concentration using the Bayesian inverse subhalo abundance matching scheme of Yasin et al. (2022, section 3.3), sampling over  $\sigma_{\text{AM}}$  and  $\beta$ .

### 3.7 The Kullback–Leibler divergence

The Kullback–Leibler divergence (Kullback & Leibler 1951) can be used to quantify the information gain in an experiment in going from the prior distribution to the posterior in units of bits

$$D_{\text{KL}}(P \parallel \pi) = \int_{\theta} \mathcal{P}(\theta) \log_2 \left( \frac{\mathcal{P}(\theta)}{\pi(\theta)} \right) d\theta. \quad (23)$$

It quantifies the similarity between  $\mathcal{P}(\theta)$  and the reference distribution  $\pi(\theta)$ . In information theory terms it is the excess surprise when using  $\mathcal{P}(\theta)$  compared to  $\pi(\theta)$ . It is the appropriate metric to use when comparing the improvement on precision in constraints between two experiments (Buchner 2022), as it takes into account the full probability distributions, as opposed to comparing a summary statistic such as the  $2\sigma$  credible interval. However, this comes at the expense of ease of interpretation. An intuitive example is an experiment with a flat prior that produces a flat posterior that has a  $k$  times smaller hypervolume. In this case  $D_{\text{KL}} = \log_2(k)$ .

To calculate  $D_{\text{KL}}$ , kernel density estimation (KDE) is used to estimate the posterior probability distribution. We use the fastKDE algorithm (O’Brien et al. 2014, 2016), which selects the kernel and bandwidth based on the criteria of Bernacchia & Pigolotti (2011). We ensure that  $D_{\text{KL}}$  is converged with respect to the number of Markov chain Monte Carlo (MCMC) samples by checking that our results do not change when using a shorter or longer chain.

In Fig. 1 we plot  $D_{\text{KL}}$  against the 2D credible interval size for one of our runs, showing the strong correlation between them. Two factors cause a scatter between  $D_{\text{KL}}$  and the size of a contour. Firstly two posteriors with the same size  $2\sigma$  contours will have a different  $D_{\text{KL}}$  if the rest of their contours are different. The prior on  $M_{\text{tot}}$  is also a function of the galaxy's  $M_{\text{bar}}$ .  $D_{\text{KL}}$  is dependent on the size of the prior. Our prior bounds are well motivated for mass, and the lower bound of concentration. However, the upper bound of concentration is arbitrary. However we are interested in the relative  $D_{\text{KL}}$  between

different measures, so our conclusions are not sensitive to the choice of prior.

### 3.8 A predictive model for $D_{\text{KL}}$

We aim to study the dependence of  $D_{\text{KL}}$  on the properties of the measurement and the properties of the galaxy. To do this we build a predictive model for  $D_{\text{KL}}$  using the ExtraTrees algorithm (Pedregosa et al. 2011). We optimize the hyperparameters through a grid search with 5-fold cross-validation (see Kohavi 1995). The features are the set of galaxy properties listed in the SPARC data base. In addition, when fitting using the full RC, we add the following features that describe the details of the galaxy and RC:  $N$  (the number of RC data points);  $R_{\text{out}}$  (the radius of the outermost data point);  $R_{\text{out}}/R_{\text{eff}}$  (the ratio of the radius of the outermost data point to the effective radius of the galaxy);  $\frac{1}{N} \sum_i V_{\text{obs},i}/V_{\text{bar},i}$  (the mean ratio of the observed velocity to the baryonic circular velocity, which quantifies the mean dark matter dominance);  $V_{\text{obs}}(r)/V_{\text{bar}}(r)$  at the radii  $R_{\text{out}}$ ,  $R_{\text{disk}}$ , and  $R_{2,2}$  (this quantifies the dark matter dominance at different points in the galaxy); the summary statistics and their uncertainties;  $\delta V_{\text{out}}/V_{\text{out}}$  (the uncertainty on the outermost data point);  $\frac{1}{N} \sum_i \delta V_{\text{obs},i}/V_{\text{obs},i}$  (the mean velocity uncertainty). When fitting using individual summary statistics, as most of the above features are not relevant, we only add the summary statistic and its uncertainty, as well the ratio of the summary statistic to the baryonic circular velocity at the corresponding radius e.g.  $V_{\text{max}}/V_{\text{bar}}(R_{\text{max}})$ .

To find which features are most important in determining  $D_{\text{KL}}$ , we use the feature importance analysis method of Stiskalek et al. (2022, section 3.6). Features are added to the list of features used to train the ExtraTrees regressor one at a time, with the feature added at each increment the one that yields the greatest improvement in accuracy. This produces a list of features, ranked from most important (added first) to least important (added last), and the new accuracy after their inclusion. This method avoids the ambiguities associated with correlated features. Due to the small sample size, we divide the sample into 10 and calculate predictions for each subsample using a regressor trained on the rest of the samples. The accuracy of the model's predictions are assessed using the coefficient of determination (Draper & Smith 1998)

$$R^2 = 1 - \frac{\sum_i (y_{i,\text{true}} - y_{i,\text{pred}})^2}{\sum_i (y_{i,\text{true}} - \hat{y}_{\text{true}})^2}, \quad (24)$$

where  $y_{i,\text{true}}$  is the test set value,  $y_{i,\text{pred}}$  the corresponding prediction, and  $\hat{y}_{\text{true}}$  the mean test set value.  $R = 1$  corresponds to perfect accuracy, and  $R = 0$  to a model that always predicts  $\hat{y}_{\text{true}}$  irrespective of the data.

## 4 RESULTS

### 4.1 Summary statistics

#### 4.1.1 Overview

In our primary analysis we wish to study the dependence of the KL divergence ( $D_{\text{KL}}$ ) on the type of measurement, properties of the measurement, and properties of the galaxy. In Fig. 2, we show the distribution of  $D_{\text{KL}}$  when fitting to the different types of measurement in the kinematic inference: the full RC,  $W_{p20}$ , or the summary statistics (see Table 1). The full rotation curve produces the tightest constraints, with a fairly flat distribution of  $D_{\text{KL}}$  between 4 and 10 bits (corresponding roughly to posteriors that are 16 and 1000 times smaller than the prior). The broad distribution of  $D_{\text{KL}}$  is due to

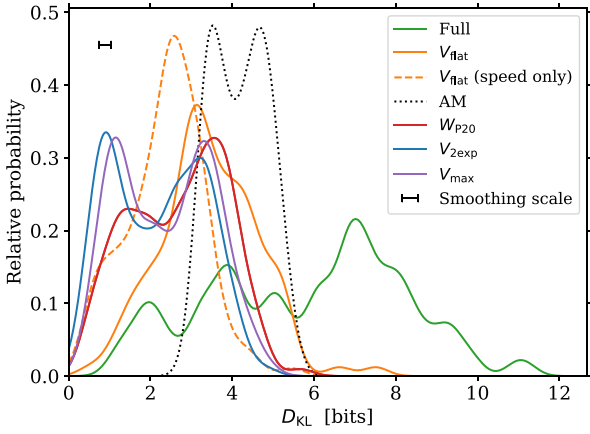


**Figure 2.** Kernel density estimation plots showing the distribution of the Kullback–Leibler divergence ( $D_{\text{KL}}$ ) for the different types of measurement, smoothed with a Gaussian kernel with a standard deviation of  $0.3 D_{\text{KL}}$  to remove unphysical small-scale noise. The full rotation curve (‘Full’) contains the most information. The single point summary statistics ( $W_{\text{p}20}/V_{\text{max}}/V_{2.2}$ ) contain much less information and are similar to each other.  $V_{\text{flat}}$  has much less information than the full RC, albeit more than other summary statistics, showing the importance of the inner parts of the RC in constraining the shape of the halo and breaking the degeneracy between mass and concentration. Abundance matching has more information than any measure except the full RC.

the massive variation both in measurement properties and galaxy properties across the sample. The summary statistics and  $W_{\text{p}20}$  produce similar distributions in  $D_{\text{KL}}$ , with a minimum of close to 0 bits (meaning the posterior is similar to the prior) and a maximum of 6 bits (approximately half that of the full RC fits).  $V_{\text{flat}}$  has a higher mean  $D_{\text{KL}}$  than the other summary statistics. We also show the distribution of  $D_{\text{KL}}$  from abundance matching, which is narrow and has a mean 1–2 bits higher than the summary statistics.

We use the `ExtraTrees` algorithm to construct a predictive model for  $D_{\text{KL}}$  and carry out a feature importance analysis (as described in Section 3.8) and show the results in Fig. 3. The model is moderately predictive, with an accuracy of  $R_2 = 0.77$ . The most important features for predicting  $D_{\text{KL}}$  are, in descending order of importance: the number of data points  $N$ , the uncertainty on the outermost measured velocity  $\delta V_{\text{out}}/V_{\text{out}}$ , the fractional uncertainty on inclination  $\delta i/i$ , the mean ratio of the observed velocity to baryonic circular velocity  $\overline{V_{\text{obs}}/V_{\text{bar}}}$  and the ratio of the radius of the outermost data point to the effective radius  $R_{\text{out}}/R_{\text{eff}}$ . We reiterate that the uncertainties on  $V_{\text{obs}}$  do not include a contribution from inclination – which is treated separately.

As illustrative examples, in Fig. 4 we show the RCs and posteriors of F574-1, a low surface-brightness galaxy, and NGC4157, an intermediate mass spiral galaxy. F574-1 is an example of a galaxy that is dark matter dominated. Its RC gradually rises and levels off to a flat part close to the last measured point. NGC4157 is baryon-dominated in its inner parts, with an RC that sharply rises to a maximum velocity that corresponds to the peak in the stellar velocity, before declining slightly to the flat part. Both galaxies have a similar number of data points, and uncertainties on observed distance and inclination. In general dark matter dominated galaxies have tighter constraints on halo properties, as when  $V_{\text{bar}}$  is low relative to  $V_{\text{obs}}$ , the uncertainties on  $V_{\text{bar}}$  (which are set by the uncertainties on the mass-to-light ratios) are less important. The RC of F574-1 is also sampled further out into

the halo (relative to the virial radius) than NGC4157, contributing to its tighter constraints.

We note that stellar mass and surface brightness, which were input features to our feature importance analysis, do not appear among the features identified as important for predicting  $D_{\text{KL}}$ . This is because, although they are correlated with the dark matter fraction, they do not themselves directly impact the strength of the constraints on halo properties. Once  $\overline{V_{\text{obs}}/V_{\text{bar}}}$  (when fitting to the full RC) or  $V_{\text{max}}/V_{\text{bar}}(R_{\text{max}})$  (when fitting to  $V_{\text{max}}$ ) are selected, adding stellar mass or surface brightness does not improve predictivity further.

#### 4.1.2 $W_{\text{p}20}$ , $V_{2.2}$ , $V_{\text{max}}$

Using either  $W_{\text{p}20}$ ,  $V_{2.2}$ , and  $V_{\text{max}}$  in the inference produces posteriors that are very similar in shape for most galaxies. We show the posteriors for  $W_{\text{p}20}$  in Fig. 4. As we have assumed the halo is spherically symmetric, the circular velocity due to the halo depends solely on its enclosed mass. This results in a complete degeneracy between the halo mass and concentration for  $W_{\text{p}20}/V_{2.2}/V_{\text{max}}$ , which do not constrain the shape of the RC. For the dark matter dominated F574-1, the posteriors are simply a band corresponding to the additional circular velocity required from the dark matter to generated the observed  $W_{\text{p}20}/V_{2.2}/V_{\text{max}}$ , thickened by its observational uncertainty and the uncertainties on  $i$ ,  $D$ , and  $\Upsilon_{\text{disc/bulge}}$ .

For NGC4157 the constraints on halo properties from  $W_{\text{p}20}/V_{2.2}/V_{\text{max}}$  are extremely weak, as the baryons alone can generate the observed values of these summary statistics. Therefore a large range of haloes are compatible with observation, as long as they do not significantly change: the mass enclosed within the H I disc for  $W_{\text{p}20}$ ; the maximum observed velocity for  $V_{\text{max}}$ ; the velocity at  $R_{2.2}$  for  $V_{2.2}$ . These three criteria result in similar constraints: a halo must have mass or concentration low enough such that there is no significant halo mass at lower radii. In the case of  $W_{\text{p}20}$ , the degeneracy between mass and concentration can be broken by fitting the full H I flux profile rather than just the linewidth, as an extended, flat RC produces a very different H I profile to a RC that peaks and then declines (as occurs with very low mass/concentration haloes). We leave this to future work.

The mean  $D_{\text{KL}}$  for  $W_{\text{p}20}/V_{\text{max}}/V_{2.2}$  is 2.76/2.41/2.27. In Fig. 3, we present the  $D_{\text{KL}}$  feature importance analysis for  $V_{\text{max}}$  only.  $V_{\text{max}}$  is chosen because it is available for more galaxies than  $W_{\text{p}20}$  and  $V_{2.2}$ , but all three give similar results. The important features are, in descending order:  $V_{\text{max}}/V_{\text{bar}}(R_{\text{max}})$  (which measures the dark matter dominance at  $R_{\text{max}}$ ),  $\delta V_{\text{max}}/V_{\text{max}}$ , its fractional uncertainty, and  $\delta i/i$ . We interpret the ordering of the mean  $D_{\text{KL}}$  for the three measurements as being due to the dark matter dominance of the region probed by each quantity. The H I disc extends beyond  $R_{2.2}$ , and so probes the RC in the more dark matter-dominated outer regions. For most galaxies in our sample,  $V_{\text{max}}$  coincides with the outer point of the RC (as in F574-1), which is typically beyond  $R_{2.2}$ . However for the galaxies with baryon-dominated inner regions such as NGC4157  $V_{\text{max}}$  roughly coincides with  $R_{2.2}$ . Hence, the mean  $D_{\text{KL}}$  for  $V_{\text{max}}$  is between  $W_{\text{p}20}$  and  $V_{2.2}$ .

#### 4.1.3 $V_{\text{flat}}$

$V_{\text{flat}}$  has higher mean  $D_{\text{KL}}$  than  $W_{\text{p}20}$ ,  $V_{\text{max}}$ , and  $V_{2.2}$ . Its posteriors (see Fig. 4) are either a band similar to  $W_{\text{p}20}$  (NGC4157) or a truncated band (F574-1). There are two distinct contributors to the constraining power on halo properties from the  $V_{\text{flat}}$  statistic. The first is that  $M_{\text{halo}}$  and  $c_{0.1}$  must generate an RC that meets the flatness criterion. If this

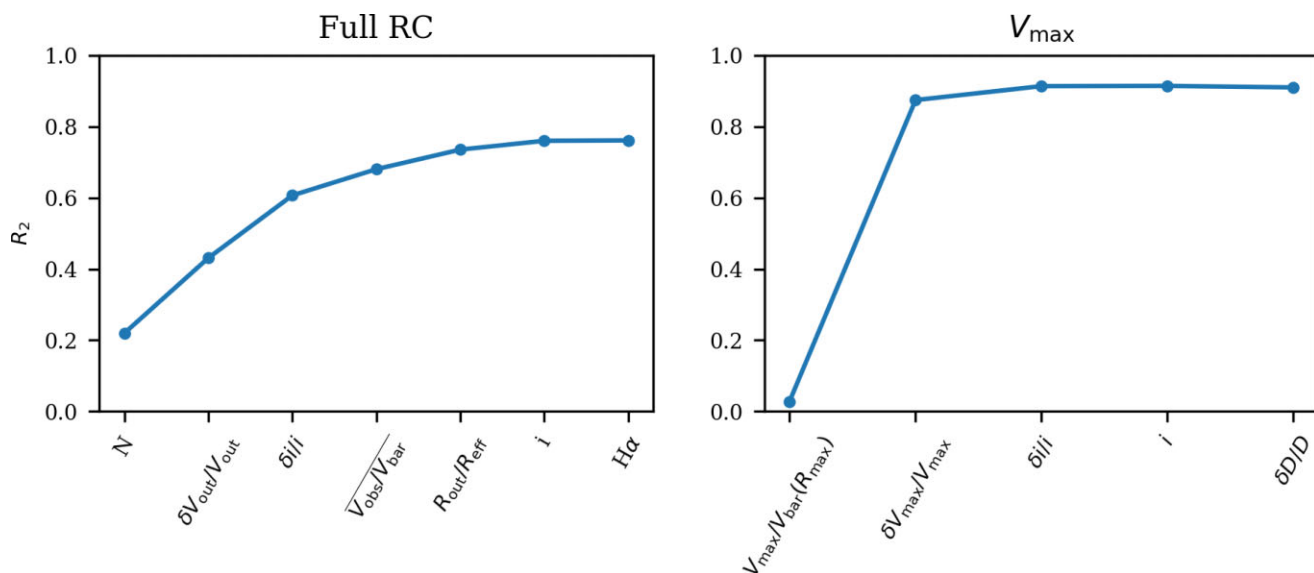


**Figure 3.** The important features for predicting the KL divergence ( $D_{\text{KL}}$ ) from fitting to the full rotation curve (left-hand panel) and fitting to  $V_{\text{max}}$  (right-hand panel) using an ExtraTrees regressor. Features are added left to right in the order which maximizes accuracy, as described in Section 3.8. No features are predictive on their own, but for the full rotation curve the combination of number of data points  $N$ , the fractional uncertainty on the outermost measured velocity  $\delta V_{\text{out}}/V_{\text{out}}$ , the fractional uncertainty on inclination  $\delta i/i$ , and the mean ratio of observed rotational velocity to baryonic circular velocity  $V_{\text{obs}}/V_{\text{bar}}$  (a measure of dark matter dominance) give reasonable accuracy, with  $R^2 = 0.77$ . For  $V_{\text{max}}$  a combination of  $V_{\text{max}}/V_{\text{bar}}(R_{\text{max}})$  and the fractional uncertainty  $\delta V_{\text{max}}/V_{\text{max}}$  give good accuracy ( $R^2 = 0.9$ ). The full list of features used in our analysis are described in Section 3.8, but includes all galaxy properties (such as stellar mass) given in the SPARC data base, as well as additional features characterizing the rotation curve (such as  $H\alpha$ , a binary variable for whether or not a galaxy has  $H\alpha$  kinematic data.).

is met, then the velocity of the flat part of the model RC must also be equal to the observed  $V_{\text{flat}}$ . The second criteria is similar to the summary statistics  $V_{2.2}$  and  $V_{\text{max}}$ , in that it simply requires one part of the RC to be a certain value, resulting in a degenerate band posterior. It is the flatness criterion that can truncate the band, as it does for F574-1.

To demonstrate the behaviour of the flatness criterion in isolation, in Fig. 4 we show the regions for which the RC is considered flat in grey. The shape of the RC depends on the parameters describing the baryons, so we consider a given  $M_{\text{tot}}, c_{0.1}$  to meet the flatness criterion if the probability of the RC being flat is  $> 34$  per cent (i.e.  $1\sigma$ ) when marginalizing over  $D$  and  $\Upsilon$ . A much smaller region of the  $M_{\text{tot}}, c_{0.1}$  prior is considered flat for F574-1 than NGC4157. This is because for NGC4157 the RC with baryons alone is considered flat, as it is gently declining over many disc scale lengths. But generating a flat RC for F574-1 requires a dark matter halo that is both dominant over the baryonic component and has high enough concentration to have reached the gently declining ‘flat’ part by the outer most RC point.

To separate the second criteria out from the flatness requirement, we calculate  $D_{\text{KL}}$  for a new summary statistic:  $V_{\text{flat}}$  (speed only). This is a single data point that is the mean speed of the flat part of the RC, occurring at its mean radius, without any flatness requirement. We see in Fig. 2 that the  $D_{\text{KL}}$  for  $V_{\text{flat}}$  (speed only) are similar to  $W_{p20}$ ,  $V_{\text{max}}$ , and  $V_{2.2}$ . This exercise demonstrates the extra constraining power that comes from observing a flat rotation curve over its length, compared to just measuring a single point from it.

We train an ExtraTrees regressor on  $D_{\text{KL}}$  for  $V_{\text{flat}}$ , but found it to be poorly predictive. This is due to difficulty in predicting the size of the region for which the flatness criterion is met, which depends on the detailed shape of the circular velocity due to the baryons.

#### 4.2 $D_{\text{KL}}$ as a function of measurement properties

In the feature importance analysis the uncertainties on inclination and velocity were found to be important predictors of  $D_{\text{KL}}$ . We now isolate their effect on  $D_{\text{KL}}$  for the full RC by scaling their uncertainties by a constant factor  $s$ , i.e.  $\delta V_{\text{obs, scaled}} = s\delta V_{\text{obs}}$  or  $\delta i_{\text{obs, scaled}} = s\delta i_{\text{obs}}$ , and repeating the inference. We do this for  $\delta V_{\text{obs}}$  and  $\delta i$  separately, for a range of values of  $s$ . We also apply the same procedure to the scatter on the prior of  $\Upsilon_{\text{disc/bulge}}$  (changing it for both disc and bulge simultaneously).

We exclude bad fits using the residual analysis described in Section 3.5. To ensure we use the same sample for all three quantities, galaxies are only included if they are not bad fits for any value of  $s$  for all of  $V_{\text{obs}}$ ,  $i$ , and  $\Upsilon_{\text{disc/bulge}}$ . With a minimum value of  $s = 0.25$  (the fits are worst for lower  $s$ ), this leaves 98 galaxies in the sample. We show their  $D_{\text{KL}}$  as a function of  $s$  in Fig. 5.  $D_{\text{KL}}$  shows the greatest dependence on the velocity uncertainties, and is relatively flat for the rest. The rate of increase in  $D_{\text{KL}}$  steepens as  $s$  decreases for  $\delta V_{\text{obs}}$  and  $i$ .

$R_{\text{out}}$  was identified as an important feature for predicting  $D_{\text{KL}}$ . It is set by the minimum H I surface density probed by the observation. We study the effect of varying the minimum H I density on  $D_{\text{KL}}$ , by repeating the inference with modified RCs that only include data points at radii where the H I surface density is above a chosen minimum value, which we vary. In this analysis we include only galaxies that each have a  $\Sigma_{\text{HI}}(r)$  that fully spans the range 1–8  $M_{\odot}/\text{pc}^2$ , and which do not have  $H\alpha$  observations, leaving 45 galaxies. The  $D_{\text{KL}}$  for this sample is shown in Fig. 6. If one knew the uncertainty on  $\Sigma_{\text{HI}}$ , an alternative approach would be to vary the minimum signal-to-noise ratio rather than the surface density.



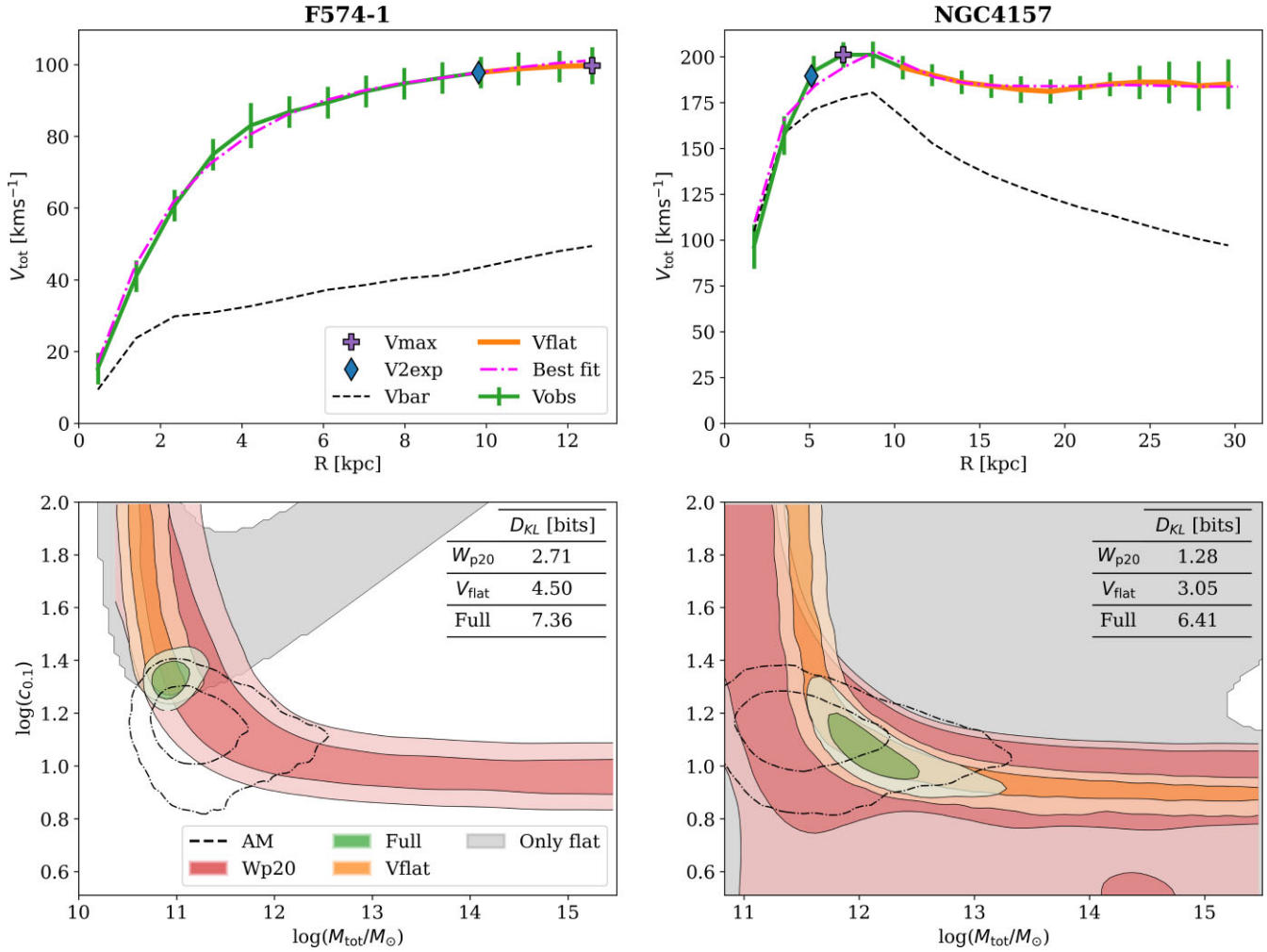


**Figure 4.** Comparison between observed and model rotation curves (*top panels*), and the posteriors in mass–concentration space for F574-1 (*left-hand panel*), a low-surface brightness galaxy, and NGC4157 (*right-hand panel*), an intermediate mass spiral galaxy. Different colours in the bottom panel show posteriors computed from fitting to the full rotation (green), fitting to the HI linewidth  $W_{\text{p20}}$  (red) and fitting to the  $V_{\text{flat}}$  summary statistic (orange, see Section 3.2). The grey shows the posterior from just requiring that the rotation curve flatness condition be met, without matching the actual value of  $V_{\text{flat}}$ . The  $D_{\text{KL}}$  of each posterior is shown on the right. The posteriors for  $V_{\text{max}}$  and  $V_{2.2}$  are not shown, but are similar to  $W_{\text{p20}}$ . The abundance matching posterior for each galaxy is also shown for comparison.

### 4.3 Halo profile comparison

We now study the constraining power of observations on whether a halo has a cusp or a core. In contrast to  $D_{\text{KL}}$ , we found that it was not possible to generate a decently predictive model for the precision of the inner slope constraints from the galaxy/RC features. This is likely because the relationship between galaxy/RC properties and the precision of inner slope constraints is more complicated than for  $D_{\text{KL}}$ , and so a larger sample size is required to generate a predictive model. Therefore, we instead focus on analysing how varying individual features affect the precision of the inner slope constraints.

In the  $D_{\text{KL}}$  analysis  $\delta V_{\text{obs}}$  was found to be the most important measurement uncertainty. Therefore we study the dependence of the likelihood ratio test between an NFW and Burkert profile on  $\delta V_{\text{obs}}$ , using the same uncertainty scaling procedure as above. We plot the resulting distribution of likelihood ratios in Fig. 7. We interpret a likelihood ratio greater than 100 as one halo profile being significantly favoured over the other. For  $s = 1$  (no scaling) this occurs

for around 30 per cent of galaxies, with most favouring Burkert. For  $s = 2$  this drops to 15 per cent, and for  $s = 0.5$  it rises to 70 per cent.

Another way of looking at this is to examine how much constraining power an observation has on the shape parameter of three parameter halo profiles. The  $\alpha$  parameter of the gNFW profile controls the gradient of the inner slope. A cusped profile has  $\alpha = 1$  and a cored profile  $\alpha = 0$ . We repeat the uncertainty scaling procedure above, but this time fitting a gNFW profile instead. The uncertainty on the marginalized  $\alpha$  parameter (which we take to be its standard deviation,  $\text{std}(\alpha)$ ) measures how well the inner slope is constrained. A galaxy with a smaller uncertainty on  $\alpha$  has a better known inner halo shape, with  $\Delta\alpha = 1$  the difference between a cored and a cusped ( $1/r$ ) inner profile. We study the distribution of  $\text{std}(\alpha)$  for the sample as a function of  $s$  in Fig. 7. The mean scatter on  $\alpha$  only drops below 0.2 for  $s \sim 0.6$ . In the right column of Fig. 7, we repeat the same halo profile comparison analysis as above, but this time varying the minimum HI density instead  $s$ . We find the dependence is much weaker than for  $\delta V_{\text{obs}}$ .

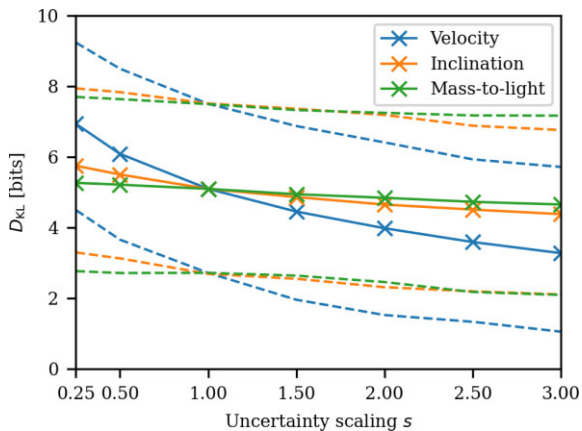


**Figure 5.** The dependence of  $D_{\text{KL}}$  on the uncertainties on velocity, inclination, and mass-to-light ratio. At each point, the uncertainties are scaled on either the velocities, the inclination, or the mass-to-light ratios on the bulge and disk by a constant factor  $s$  (such that  $\delta' = s\delta$ ) and the  $D_{\text{KL}}$  from fitting to the full rotation curve is recalculated for each galaxy. Any galaxy that is considered underfit (see 3.5) for any value of  $s$  for any of velocity/inclination/mass-to-light is excluded from this analysis. Therefore,  $D_{\text{KL}}$  is calculated for the same sample of 98 galaxies for all points. The solid lines show the mean of  $D_{\text{KL}}$  at each value of  $s$  (marked by crosses), and the dashed lines show the 16th and 84th quantiles of the distribution.  $D_{\text{KL}}$  is most dependent on the velocity uncertainties.

Another possibly important factor for determining the inner slope constraints is whether or not a galaxy has  $\text{H}\alpha$  observations. We split the sample in two, and find galaxies with  $\text{H}\alpha$  have a mean  $\text{std}(\alpha)$  of 0.23, but those without have a mean of 0.3. We have checked the two populations of galaxies do not significantly differ with respect to other variables that drive the constraints on  $D_{\text{KL}}$ , and so conclude that adding  $\text{H}\alpha$  observations moderately reduces the uncertainty on the inner slope (comparable to halving the velocity uncertainties from their fiducial values).

## 5 DISCUSSION

### 5.1 Predicting information gain

Constraining halo mass and concentration from fits to rotation curve data is routine procedure in the study of late-type galaxies. However, to our knowledge, this study is the first to formally quantify the precision of the constraints and study their variation with galaxy and measurement properties. For the SPARC sample, we found massive variation in precision on  $M_{\text{tot}}$  and  $c_{0.1}$  when fitting to the full RC, ranging from 1 to 11 bits of information gain. This range is equivalent to the difference between a flat prior shrinking to a flat posterior by only a factor of 2 ( $2^1$ ) compared to  $\sim 2000$  ( $2^{11}$ ). We created a predictive model for  $D_{\text{KL}}$  using the `EXTRA`Trees algorithm, and conducted a feature importance analysis to identify the galaxy and measurement properties that are the strongest predictors of information gain. The measurement properties are, in descending order of importance: the number of data points  $N$ , the fractional uncertainty on the outermost measured velocity  $\delta V_{\text{out}}/V_{\text{out}}$ , the fractional uncertainty on inclination  $\delta i/i$ , and the radius of the outermost measured velocity normalized by the effective radius  $R_{\text{out}}/R_{\text{eff}}$ . The only important galaxy property is  $\overline{V_{\text{obs}}/V_{\text{bar}}}$ , a measure of the dark matter dominance.  $N$  ranks more highly than both the maximum radius of the RC (although the two are positively correlated, with a Spearman coefficient of 0.58) and whether or not a galaxy has  $\text{H}\alpha$  data. This shows the

importance of sampling at many points across the RC to constrain the shape.

The moderate predictivity of our model ( $R^2 = 0.77$ ) is part due to the small sample size, and part due to the input features not fully capturing the full details of the RC and the distribution of the baryons. For example  $N$  does not account for the autocorrelation of the RC, and  $\overline{V_{\text{obs}}/V_{\text{bar}}}$  is only an average. Our model is more predictive for the fits to the single data point summary statistics,  $W_{p20}$ ,  $V_{2.2}$ , and  $V_{\text{max}}$ , with the latter giving  $R^2 = 0.9$  and depending only on the uncertainty on  $V_{\text{max}}$  and  $V_{\text{max}}/V_{\text{bar}}(R_{\text{max}})$ , a measure of dark matter dominance.

Our feature importance analysis only ranks the measurement properties by importance. In order to quantify the size of their effect on  $D_{\text{KL}}$ , we varied the uncertainties on velocity and inclination whilst holding the rest of the inference constant. We also varied uncertainties on the mass-to-light ratios  $\Upsilon_{\text{disc}}$  and  $\Upsilon_{\text{bulge}}$ , applied in our model through the priors. We find that the constraints are most dependent on the velocity uncertainties, with the inclination and mass-to-light showing only weaker dependence. In Fig. 6, we calculated the dependence of  $D_{\text{KL}}$  on the minimum H I density probed (which sets the maximum radius of the RC). Reducing the minimum density by  $1 M_{\odot}/\text{pc}^2$  yields an additional 0.4 bits of information gain. In order to investigate whether this dependence on the minimum H I density simply mirrors the strong dependence on  $N$  found earlier (Fig. 3), we also plotted  $D_{\text{KL}}/N$  for the different runs (not shown), and found no strong trend with the minimum H I density. This suggests that the observed trend in  $D_{\text{KL}}$  with minimum H I density is driven primarily by  $N$ , rather than say the points in the outer RC (where the H I density is lowest) yielding disproportionately more information. This concurs with our earlier finding that  $R_{\text{out}}/R_{\text{eff}}$  is a less important feature than  $N$ .

Our results can inform future survey design, by highlighting which features of the measurement should be prioritized for optimization. The main way to improve constraints is of course to use longer integration times or higher instrument sensitivity, which would increase the number of data points (Staveley-Smith & Oosterloo 2015). However, specific optimizations are possible. The beam size sets the maximum resolution. At fixed sensitivity/integration time, there is a trade off between minimum H I density that can be probed (i.e. the maximum radius) and resolution, although this can be altered with adaptive smoothing techniques in post-processing (Briggs 1995). Reducing the velocity uncertainties would require improving the model used to determine the velocities and/or increasing the spectroscopic resolution. SPARC inclinations are produced as output of the fits to the 2D velocity field (Lelli et al. 2016a), so the uncertainties would be reduced by improving the velocity map. Inclination can also be calculated using the ellipticity of the H I zeroth-moment map (Ponomareva et al. 2021), including forward modelling it to the datacube (Mancera Piña et al. 2021), or more imprecisely using optical data. Kourkchi, Tully & Courtois (2022) recently used a combination of machine learning and citizen science to improve inclinations from optical data. Schombert, McGaugh & Lelli (2022) use stellar population models to study the variation of the uncertainty on  $\Upsilon$  with the passband, and the available morphology and colour information.

### 5.2 Summary statistics

We compared the information gain when constraining halo parameters using the full RC, summary statistics or the H I linewidth  $W_{p20}$ . Our feature importance analysis found the degree of dark matter dominance at the radius of the velocity measurement was the most

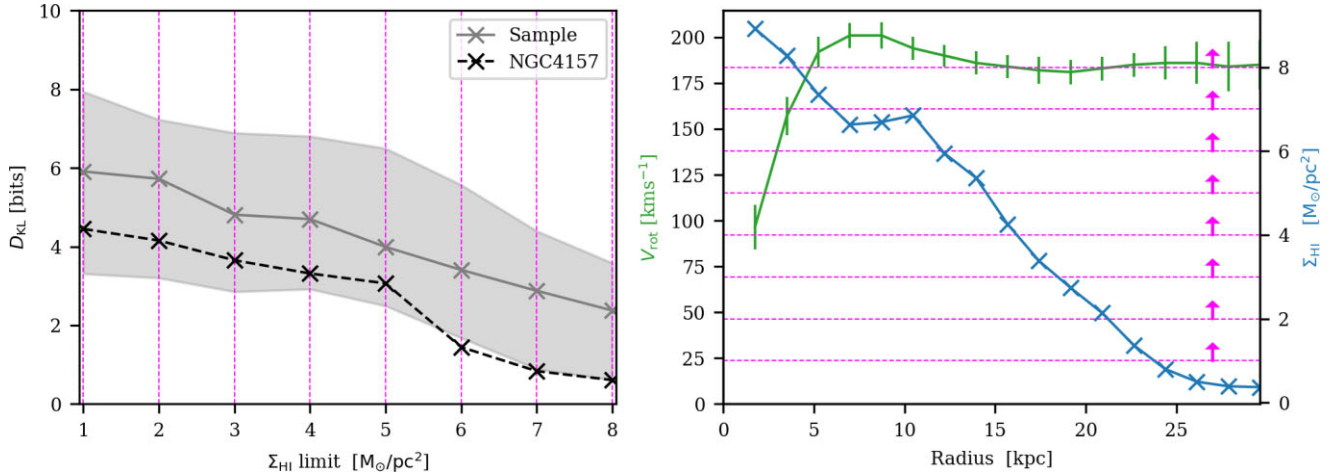


**Figure 6.** The dependence of  $D_{\text{KL}}$  (grey line, sample mean; band, 16th and 84th quantiles) on the minimum HI surface density probed  $\Sigma_{\text{HI},\text{min}}$  (left-hand panel). The procedure for varying  $\Sigma_{\text{HI},\text{min}}$  is illustrated for a single galaxy (NGC4157) in the right-hand panel: for each value of  $\Sigma_{\text{HI},\text{min}}$  (pink lines), only the data points of the rotation curve (blue) at radii where  $\Sigma_{\text{HI}} > \Sigma_{\text{HI},\text{min}}$  (i.e. green > pink) are used in the inference. The  $D_{\text{KL}}$  for NGC4157 is shown as a dashed line in the left-hand panel. This analysis is only applied to the subsample of 54 galaxies that each have an HI surface density profile that spans all the way from 1 to 8  $\Sigma_{\text{HI}}/M_{\odot}\text{pc}^{-2}$ . For this sample,  $D_{\text{KL}}$  increases strongly (with an approximately linear relationship) as  $\Sigma_{\text{HI},\text{min}}$  is reduced and the lower surface density regions towards the outskirts of the galaxy are added to the observation.

important factor in determining  $D_{\text{KL}}$ . The ranking of mean  $D_{\text{KL}}$  for the summary statistics from highest to lowest is  $\{V_{\text{flat}}, W_{p20}, V_{\text{max}}, V_{2.2}\}$ , which reflects how far out into the halo each measurement probes, and hence the degree of dark matter domination. L19 calculated the intrinsic scatter of the baryonic Tully-Fisher relationships (BTFRs) constructed using the different summary statistics as the velocity measure. For the ones studied in this paper, they found  $\{V_{\text{flat}}, W_{p20}, V_{\text{max}}, V_{2.2}\}$  had an intrinsic orthogonal scatter of  $\{0.026, 0.035, 0.040, 0.070\}$  respectively, which is the inverse ordering of  $D_{\text{KL}}$ . L19 interpret the amount of scatter to be negatively correlated with the closeness of the summary statistic to the true flat value of the rotation curve (as opposed to the observed  $V_{\text{flat}}$ , which is limited by maximum radius probed in some galaxies). Hence, it is not surprising that the mean information content on halo properties from each measurement is negatively correlated with the scatter of their respective BTFRs.

In this work we chose not to apply a prior based on the mass–concentration relationship from dark matter-only simulations. Although this would have helped break the degeneracy between mass and concentration (see also Section 1), it would also have imported assumptions from  $N$ -body simulations and galaxy formation theory (assembly bias) which we prefer to avoid. However, we now qualitatively discuss the effect this prior would have on our results. Applying the mass–concentration prior increases  $D_{\text{KL}}$  significantly for all galaxies, with the effect greatest when using relatively weak data such as summary statistics for which the mass–concentration degeneracy is especially pronounced. Applying the prior whilst assuming a cuspy profile leads to a finite constraint on halo mass even when using such summary statistics (this is studied for linewidths in more detail in Yasin et al. 2022). However for many galaxies, even with the mass–concentration prior applied there is still a strong remaining degeneracy (e.g. NGC4157 in the right-hand panel of Fig. 4), especially when assuming a cored profile. Nevertheless  $D_{\text{KL}}$  still increases significantly compared to the no-prior case, even when the degeneracy is not fully broken. It is important to bear in mind however that in this case the information gain is not purely from the kinematic data.

### 5.3 Constraining the inner halo shape

We studied the ability of observations to constraint the inner halo shape in two ways. Firstly we studied the impact of the  $\delta V_{\text{obs}}$  uncertainties on the ability to distinguish between the cored Burkert profile and cusped NFW profile using a likelihood ratio test. We found that with the unmodified velocity uncertainties, one profile was decisively favoured over another in 40 per cent of cases, with this rising to 70 per cent when the uncertainties are halved. On the other hand, when the uncertainties are doubled, one halo is only strongly favoured in only 20 per cent of galaxies. We also studied the uncertainty of the inner slope parameter  $\alpha$  when fitting a 3-parameter generalized NFW profile. With the normal SPARC uncertainties the mean  $\text{std}(\alpha)$  is  $\sim 0.3$  (the change in  $\alpha$  is 1 between a cored gNFW profile and a normal NFW profile), but there are a significant number of galaxies with  $\text{std}(\alpha) > 0.5$ . This suggests a survey with velocity measurements more precise than SPARC is necessary to precisely constrain the inner halo shape for whole samples of galaxies. We repeated the analysis varying the minimum HI density probed, and found a much weaker dependence. This demonstrates the importance of obtaining kinematic data sets with precise velocity uncertainties when targetting the cusp-core problem (see Del Popolo & Le Delliou 2021, for a review) relative to probing lower HI surface densities.

### 5.4 Comparison to literature

Saburova, Kasparova & Katkov (2016) used a sample of 14 galaxies from The HI Nearby Galaxy Survey (THINGS, Walter et al. 2008) to study the size of the uncertainties on halo parameters derived from rotation curve fitting, in particular identifying the halo concentration as often poorly constrained. The main differences to this paper are our quantification of the constraining power using the Kullback–Leibler divergence, our focus on the constraining power in the mass–concentration plane rather than the uncertainty on individual parameters, our study of the constraining power as a function of measurement and galaxy properties, and our Bayesian fitting procedure that propagates the uncertainties on galaxy parameters

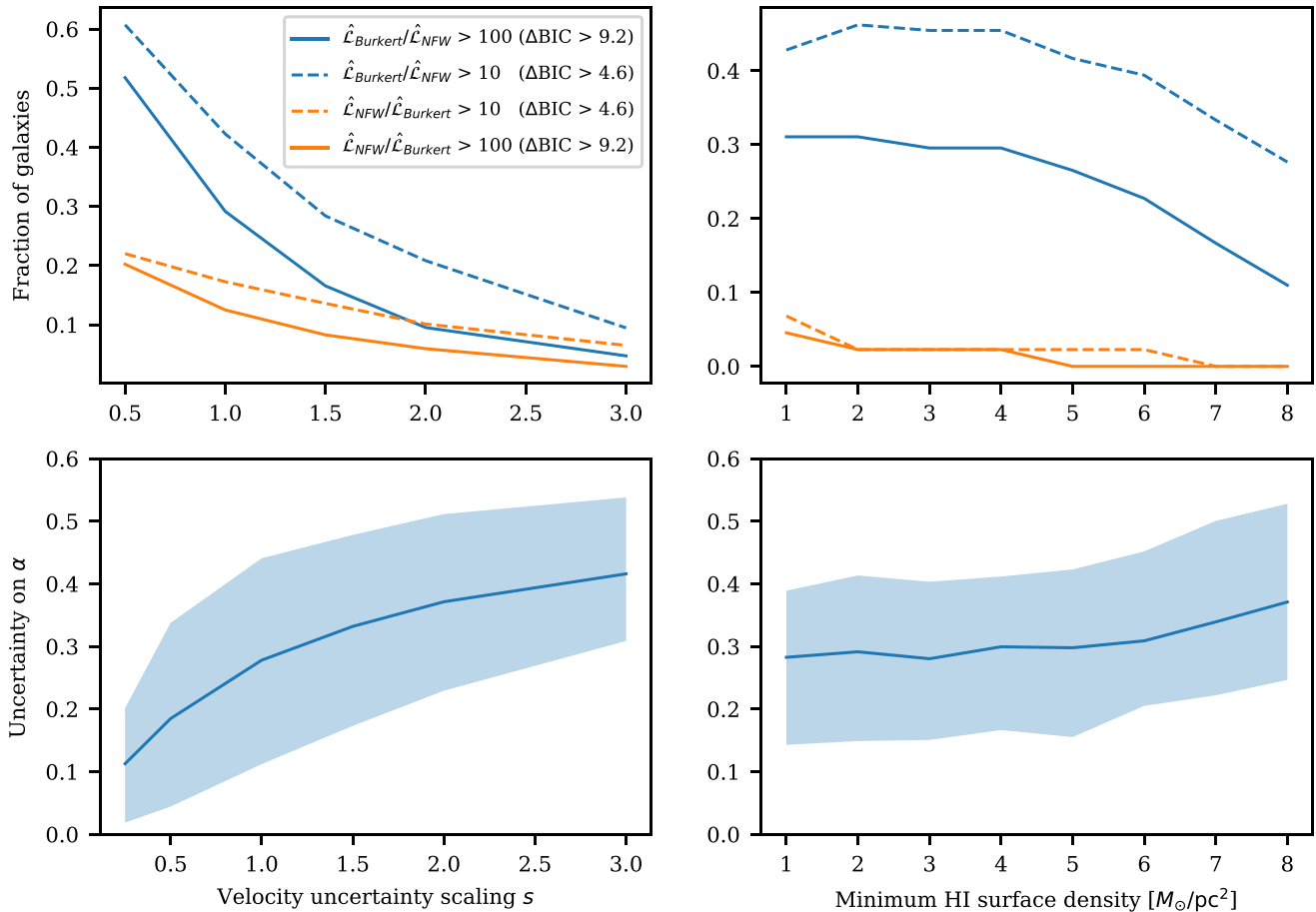


**Figure 7.** *Top panels:* The fraction of galaxies in the sample for which the ratio of the maximum likelihood estimates of the two profiles  $\hat{\mathcal{L}}_{\text{Burkert}}/\hat{\mathcal{L}}_{\text{NFW}}$  (or the inverse) is above a certain value, as a function of a multiplicative scaling  $s$  of the velocity uncertainties (*left-hand panels*, see Fig. 5) and the minimum HI surface density probed (*right-hand panels*, see Fig. 6). We interpret  $\hat{\mathcal{L}}_{\text{Burkert}}/\hat{\mathcal{L}}_{\text{NFW}} > 100$  (10) as strongly (moderately) favouring Burkert over NFW (and vice-versa). At  $s = 1$  (no scaling) one halo is strongly favoured over another in around  $\sim 40$  per cent of galaxies, with most favouring Burkert. If the velocity uncertainties are halved ( $s = 0.5$ ), this rises to 70 per cent. For reference we also show the corresponding difference in Bayesian Information Criterion. *Bottom panels:* The distribution of the uncertainties on the  $\alpha$  shape parameter from fitting a gNFW halo to the full rotation curve (solid line, mean; band, 16th and 84th quantiles in bins of  $s$ ). Both the uncertainties on  $\alpha$  and the likelihood ratios show a strong dependence on the velocity uncertainties, but a weaker dependence on the HI surface density.

into the constraints on halo properties. In agreement with Saburova et al. (2016), we find that for many galaxies the constraining power offered by rotation curves can still be relatively weak (as evidenced by the long tail to low  $D_{\text{KL}}$  for the full RC in Fig. 2).

We have highlighted the important measurement properties which should be targeted by future surveys. Identifying the observational parameters (such as integration time) required to achieve the desired measurement properties is beyond the scope of this work. Recent work has simulated spectroscopic HI observations of simulated late-type galaxies (Oman 2019), which in theory allows an end-to-end determination of the effect of observational properties such as integration time on the constraints on halo properties. However, our analysis of real observations is an important complementary approach, as simulations still struggle to produce realistic samples of rotation curves (Roper et al. 2022).

In light of increasingly expensive observations, but comparatively cheap computational resources, there are an increasing number of studies examining optimal observational strategies. For example,

two recent studies have used the Fisher-matrix formalism to quantify the information content in stellar streams (Bonaca & Hogg 2018) and the cosmic web (Kostić et al. 2022) in order to identify the best observational strategy.

## 6 CONCLUSION

We have used the Kullback–Leibler divergence ( $D_{\text{KL}}$ ) of the posterior on total mass–concentration (where total mass is equal to the halo mass plus the galaxy mass) from the prior to quantify the gain in information obtained from spectroscopic observations of the late-type galaxies of the SPARC data base. We set the observable in the kinematic inference to be either the full rotation curve, summary statistics of the rotation curve ( $V_{\text{max}}$ ,  $V_{2.2}$ ,  $V_{\text{flat}}$ ), or the linewidth of the integrated 21-cm spectrum,  $W_{p20}$ , in order to quantify the information contained in different parts of the rotation curve and different types of measurement. Further, to determine the properties of the measurements that are most important for the information gain, we study the variation on  $D_{\text{KL}}$  as we modify properties of the

rotation curve observations such as the uncertainties on velocity or the minimum HI surface density probed. Our conclusions are as follows:

(i) The full RC fitting offers a wide range of information gain for the SPARC galaxies, ranging from  $\sim 1$  to  $\sim 11$  bits. This is predominantly due to the massive range in the number of data points each rotation curve has, and the large variation in velocity uncertainties.

(ii) Fits to the summary statistics of the RCs offer much smaller gains, ranging from  $\sim 0$  to  $\sim 6$  bits, as the posteriors are degenerate in mass–concentration and run up against the prior bounds.  $V_{\text{flat}}$  offers a modest increase due to the flatness constraint. For most SPARC galaxies  $W_{p20}$ ,  $V_{\text{flat}}$ ,  $V_{2.2}$ , and  $V_{\text{max}}$  all probe regions of the rotation curve which are dark matter dominated, and hence contain similar information on the halo.

(iii) We measured  $D_{\text{KL}}$  as a function of the minimum HI surface density probed, and the uncertainties on velocity, inclination, and mass-to-light ratios. Its dependence is strongest on the minimum surface density and the velocity uncertainties. These results can be used to weigh up the increase in precision on halo constraints afforded by improving each aspect of the measurement against the associated cost.

(iv) The tightness of the constraints on the inner halo shape are strongly dependent on the velocity uncertainties, but have a much weaker dependence on the minimum HI surface density. This suggests that whilst both sensitivity and velocity uncertainties are important for obtaining tight constraints on halo properties, surveys specifically targeting e.g. the cusp-core problem should prioritize the latter.

Our study has identified the most important variables for improving the constraints on dark matter halo properties from spectroscopic observations of late-type galaxies. With forthcoming instruments set to greatly enhance our ability to probe the dark matter distribution around galaxies, in terms of number of galaxies, increasing redshift and measurement precision, these results should inform future survey design to maximize the return of knowledge on the galaxy–halo connection.

## ACKNOWLEDGEMENTS

We thank Anastasia Ponomareva, Richard Stiskalek, Johannes Buchner, and Jamie Bamber for useful inputs and discussion.

HD was supported by a Royal Society University Research Fellowship (grant no. 211046).

This project has received funding from the European Research Council (ERC) under the European Union’s Horizon 2020 research and innovation programme (grant agreement no. 693024).

For the purpose of open access, the authors have applied a Creative Commons Attribution (CC BY) licence to any Author Accepted Manuscript version arising.

## DATA AVAILABILITY

The data underlying this article will be made available on reasonable request to the corresponding author.

## REFERENCES

Adhikari S. et al., 2022, preprint (arXiv:2207.10638)  
 Andrae R., Schulze-Hartung T., Melchior P., 2010, preprint (arXiv:1012.3754)

Bernacchia A., Pigolotti S., 2011, *J. R. Stat. Soc. B*, 73, 407  
 Bonaca A., Hogg D. W., 2018, *ApJ*, 867, 101  
 Briggs D. S., 1995, PhD thesis, The New Mexico Institute of Mining and Technology  
 Bryan G. L., Norman M. L., 1998, *ApJ*, 495, 80  
 Buchner J., 2022, *Res. Notes Am. Astron. Soc.*, 6, 89  
 Bundy K. et al., 2014, *ApJ*, 798, 7  
 Bureau M., Carignan C., 2002, *AJ*, 123, 1316  
 Burkert A., 1995, *ApJ*, 447, L25  
 Burrage C., Copeland E. J., Millington P., 2017, *Phys. Rev. D*, 95, 064050  
 Caserano S. P. R., Shostak G. S., 1980, *A&A*, 81, 371  
 Collett T. E. et al., 2017, *ApJ*, 843, 148  
 Conroy C., Wechsler R. H., Kravtsov A. V., 2006, *ApJ*, 647, 201  
 Conselice C., Bundy K., Ellis R., Brinchmann J., Vogt N., 2004, *Proc. IAU Symp. 220*, p. 399 IAU by Astronomical Society of the Pacific, 2004  
 Courteau S., 1997, *AJ*, 114, 2402  
 Croom S. M. et al., 2021, *MNRAS*, 505, 991  
 Dalal N., White M., Bond J. R., Shirokov A., 2008, *ApJ*, 687, 12  
 Deg N. et al., 2022, *Publ. Astron. Soc. Aust.*, 39, e059  
 Del Popolo A., Le Delliou M., 2021, *Galaxies*, 9, 123  
 Di Cintio A., Brook C. B., Macciò A. V., Stinson G. S., Knebe A., Dutton A. A., Wadsley J., 2014, *MNRAS*, 437, 415  
 Di Teodoro E. M., Fraternali F., Miller S. H., 2016, *A&A*, 594, A77  
 Draper N. R., Smith H., 1998, *Applied Regression Analysis*. John Wiley and Sons, Hoboken, New Jersey  
 Dutton A. A., Macciò A. V., 2014, *MNRAS*, 441, 3359  
 Foreman-Mackey D., Hogg D. W., Lang D., Goodman J., 2013, *PASP*, 125, 306  
 Goodman J., Weare J., 2010, *Commun. Appl. Math. Comput. Sci.*, 5, 65  
 Haynes M. P. et al., 2018, *ApJ*, 861, 49  
 Iorio G., Fraternali F., Nipoti C., Di Teodoro E., Read J. I., Battaglia G., 2016, *MNRAS*, 466, 4159–4192  
 Jones G. C. et al., 2021, *MNRAS*, 507, 3540  
 Katz H., Lelli F., McGaugh S. S., Di Cintio A., Brook C. B., Schombert J. M., 2017, *MNRAS*, 466, 1648  
 Katz H., Desmond H., McGaugh S., Lelli F., 2019, *MNRAS*, 483, L98  
 Khelashvili M., Rudakovskiy A., Hossenfelder S., 2022, *MNRAS*, 523, 3393  
 Kohavi R., 1995, *Proc. Fourteenth Int. Joint Conf. Artificial Intelligence*. International Joint Conferences on Artificial Intelligence, the University of California  
 Koribalski B. S. et al., 2020, *Astrophys. Space Sci.*, 365, 118  
 Kostić A., Jasche J., Ramanah D. K., Lavaux G., 2022, *A&A*, 657, L17  
 Kourkchi E., Tully B., Courtois H., 2022, *BAAS*, 54 302.07  
 Kravtsov A. V., Berlind A. A., Wechsler R. H., Klypin A. A., Gottlöber S., Allgood B., Primack J. R., 2004, *ApJ*, 609, 35  
 Kullback S., Leibler R. A., 1951, *Ann. Math. Stat.*, 22, 79  
 Lang P. et al., 2020, *ApJ*, 897, 122  
 Lehmann B. V., Mao Y.-Y., Becker M. R., Skillman S. W., Wechsler R. H., 2016, *ApJ*, 834, 37  
 Lelli F., McGaugh S. S., Schombert J. M., 2015, *ApJ*, 816, L14  
 Lelli F., McGaugh S. S., Schombert J. M., 2016a, *AJ*, 152, 157  
 Lelli F., McGaugh S. S., Schombert J. M., 2016b, *ApJ*, 816, L14  
 Lelli F., McGaugh S. S., Schombert J. M., Desmond H., Katz H., 2019, *MNRAS*, 484, 3267 (L19)  
 Lelli F., Di Teodoro E. M., Fraternali F., Man A. W. S., Zhang Z.-Y., De Breuck C., Davis T. A., Maiolino R., 2021, *Science*, 371, 713  
 Lelli F. et al., 2023, *A&A*, 672, A106  
 Leroy A. K., Walter F., Brinks E., Bigiel F., de Blok W. J. G., Madore B., Thornley M. D., 2008, *AJ*, 136, 2782  
 Li P., Lelli F., McGaugh S. S., Starkman N., Schombert J. M., 2019, *MNRAS*, 482, 5106  
 Li P., Lelli F., McGaugh S., Schombert J., 2020, *ApJS*, 247, 31  
 Li P., McGaugh S. S., Lelli F., Schombert J. M., Pawłowski M. S., 2022, *Astronomy and Astrophysics*, 665, A143  
 Maddox N. et al., 2021, *A&A*, 646, A35  
 Mancera Piña P. E., Fraternali F., Oosterloo T., Adams E. A. K., Oman K. A., Leisman L., 2021, *MNRAS* 512 3230–3242

- Mancera Piña P. E., Fraternali F., Oosterloo T., Adams E. A. K., di Teodoro E., Bacchini C., Iorio G., 2022, *MNRAS*, 514, 3329
- Mandelbaum R., Wang W., Zu Y., White S., Henriques B., More S., 2016, *MNRAS*, 457, 3200
- Martinsson T. P. K., Verheijen M. A. W., Westfall K. B., Bershadsky M. A., Schechtman-Rook A., Andersen D. R., Swaters R. A., 2013, *A&A*, 557, A130
- Massey F. J., 1951, *J. Am. Stat. Assoc.*, 46, 68
- McGaugh S. S., 2005, *ApJ*, 632, 859
- McGaugh S. S., Schombert J. M., Bothun G. D., de Blok W. J. G., 2000, *ApJ*, 533, L99
- McGaugh S. S., Lelli F., Schombert J. M., 2016, *Phys. Rev. Lett.*, 117, 201101
- McGaugh S., Lelli F., Li P., Schombert J., 2019, *Proc. IAU*, 14, p. Cambridge University Press, Cambridge, 144
- Milgrom M., 1983, *ApJ*, 270, 365
- Mogotsi K. M., de Blok W. J. G., Caldu-Primo A., Walter F., Ianjamasimanana R., Leroy A. K., 2016, *AJ*, 151, 15
- Naik A. P., Puchwein E., Davis A.-C., Sijacki D., Desmond H., 2019, *MNRAS*, 489, 771
- Navarro J. F., Frenk C. S., White S. D. M., 1997, *ApJ*, 490, 493
- O'Brien T. A., Collins W. D., Rauscher S. A., Ringle T. D., 2014, *Comput. Stat. Data Anal.*, 79, 222
- O'Brien T. A., Kashinath K., Cavanaugh N. R., Collins W. D., O'Brien J. P., 2016, *Comput. Stat. Data Anal.*, 101, 148
- Obreschkow D., Croton D., De Lucia G., Khochfar S., Rawlings S., 2009, *ApJ*, 698, 1467
- Oh S.-H. et al., 2015, *AJ*, 149, 180
- Oman K. A., 2019, *Astrophysics Source Code Library*, record ascl:1911.005
- Oosterloo T., Verheijen M., van Cappellen W., 2010, *ISKAF2010 science meeting Proceedings of Science*, Trieste, 43
- Pedregosa F. et al., 2011, *J. Mach. Learn. Res.*, 12, 2825
- Ponomareva A. A., Verheijen M. A. W., Bosma A., 2016, *MNRAS*, 463, 4052
- Ponomareva A. A., Verheijen M. A. W., Papastergis E., Bosma A., Peletier R. F., 2018, *MNRAS*, 474, 4366
- Ponomareva A. A. et al., 2021, *MNRAS*, 508, 1195
- Posti L., Fall S. M., 2021, *A&A*, 649, A119
- Posti L., Fraternali F., Marasco A., 2019, *A&A*, 626, A56
- Read J. I., Agertz O., Collins M. L. M., 2016, *MNRAS*, 459, 2573
- Rizzo F., Vegetti S., Fraternali F., Stacey H. R., Powell D., 2021, *MNRAS*, 507, 3952
- Roper F. A., Oman K. A., Frenk C. S., Benítez-Llambay A., Navarro J. F., Santos-Santos I. M. E., 2022, *MNRAS*, 521, 1316–1336
- Saburova A. S., Kasparova A. V., Katkov I. Y., 2016, *MNRAS*, 463, 2523
- Schombert J. M., McGaugh S., 2014, *Publ. Astron. Soc. Aust.*, 31, e011
- Schombert J., McGaugh S., Lelli F., 2018, *MNRAS*, 483, 1496–1512
- Schombert J., McGaugh S., Lelli F., 2022, *AJ*, 163, 154
- Shajib A. J., Treu T., Birrer S., Sonnenfeld A., 2021, *MNRAS*, 503, 2380
- Staveley-Smith L., Oosterloo T., 2015, *Advancing astrophysics with the square kilometre array (AASKA14) Proceedings of Science*, Trieste, 167
- Stiskalek R., Bartlett D. J., Desmond H., Anbajagane D., 2022, *MNRAS*, 514, 4026–4045
- Stott J. P. et al., 2016, *MNRAS*, 457, 1888
- Taranu D. S. et al., 2017, *ApJ*, 850, 70
- Tully R. B., Fisher J. R., 1977, *A&A*, 500, 105
- Umetsu K., Broadhurst T., Zitrin A., Medezinski E., Coe D., Postman M., 2011, *ApJ*, 738, 41
- Walter F., Brinks E., de Blok W. J. G., Bigiel F., Kennicutt J., Thornley M. D., Leroy A. K., 2008, *AJ*, 136, 2563
- Wechsler R. H., Tinker J. L., 2018, *ARA&A*, 56, 435
- Yahya S., Bull P., Santos M. G., Silva M., Maartens R., Okouma P., Bassett B., 2015, *MNRAS*, 450, 2251
- Yasin T., Desmond H., Devriendt J., Slyz A., 2022, *MNRAS*, stad1183
- Zentner A., Dandavate S., Slone O., Lisanti M., 2022, *J. Cosmol. Astropart. Phys.*, 2022, 031
- Zhang K. et al., 2020, *MNRAS*, 500, 1741

This paper has been typeset from a  $\text{\TeX}/\text{\LaTeX}$  file prepared by the author.